Deposition on the Waiapu, New Zealand, continental shelf by seasonal wave- and current-supported sediment gravity flows interacting with spatially varying bathymetry

Yanxia Ma[1,*], Carl T. Friedrichs[2], Courtney K. Harris[3], L. Donelson Wright[4]

[1-3]Virginia Institute of Marine Science, College of William and Mary, P.O. Box 1346, Gloucester Point, VA 23062, USA,

[1]yma@vims.edu, [2]cfried@vims.edu, [3]ckharris@vims.edu

[4]Southeastern University Research Association, 1201 New York Ave, NW, Suite 430, Washington, DC 20005, USA, wright@sura.org

*Corresponding author

Version 7/29/09, to be submitted to Marine Geology August 2009.

Abstract

The Waiapu system provides a prototype for investigating the relative importance of wave- versus current-supported gravity flows on shelf deposition. A two-dimensional model was used to represent gravity-driven sediment transport and deposition on the Waiapu shelf, New Zealand, over an annual cycle of storm events and associated Waiapu River floods. The 12-month run, forced by WAVEWATCH III hindcasts and constrained by benthic tripod data, was divided into two portions: a low-energy period (September 2003 to May 2004) with weak waves and currents and low river discharge, and a high-energy period (May to August 2004) with stronger waves and wind-driven currents and more frequent river floods. Model results indicated that during the low-energy period, riverine sediment was trapped between the 20- and 80-m isobaths. During the high-energy period, sediment was deposited obliquely across the shelf between the 60- and 120-m isobaths. The predicted deposit locations for the low- and high-energy portions, respectively, matched well with short- and long-term observed accumulation patterns based on ^{7}Be and ^{210}Pb activity (Kniskern et al., 2009). Significant gravity flows were mainly wave-supported landward of the 60-m isobath, but became increasingly current-supported as wave orbitals decayed in deeper water. Both analytical theory and numerical results showed that wave-supported gravity currents were sensitive to local water depth and favored deposition parallel to isobaths as depth increased. In contrast, current-supported gravity currents were more sensitive to spatial variations in bathymetry, with seaward decreasing slope and embayed isobaths favoring transport convergence. We conclude

that the longer term (~100 yr), shelf-oblique mud deposit on the Waiapu shelf is mainly the result of current-supported gravity flows responding to local variations in seabed slope and curvature of isobaths.

Keywords: Waiapu River, New Zealand, Gravity-driven flow, sediment transport, sediment deposition

1. Introduction

Until the 1990s, sediment gravity flows were largely considered insignificant for the dispersal of riverine sediment across continental shelves because few shelves are steep enough to provide sufficient gravity forces to maintain autosuspension, and few river effluents are turbid enough to directly produce hyperpycnal discharges. This opinion was fundamentally challenged a decade ago by new field observations and hydrodynamic theory, as well as reexamination of existing data, which indicated that gravity flows can occur on more gently sloping continental shelves when waves and/or currents provide sufficient turbulence to develop near-bed hyperpycnal layers by sediment resuspension (Traykovski et al., 2000; Wright et al., 2001).

Three prominent examples of shelves impacted by sediment gravity flows are found seaward of the Eel, Po and Yellow Rivers. Physical and geological studies were conducted on the Eel shelf in the late 1990s as part of the STRATAFORM program (Nittrouer, 1999). One of the fundamental conclusions of STRATAFORM was that across-shelf transport of Eel sediment was dominated by wave-supported gravity flows (Ogston et al., 2000; Traykovski et al., 2000; Scully et al., 2002; Harris et al.,

2005). EuroSTRATFORM collected observations on the Po subaqueous delta from the winter 2000 to the spring 2003 (Nittrouer et al., 2004). Field and modeling results again showed that wave-supported gravity flows played an important role in moving sediment downslope offshore of the river mouth (Traykovski et al., 2007; Friedrichs and Scully, 2007). The Yellow River is characterized by extremely high sediment concentrations and is one of relatively the few rivers from which hyperpycnal discharge regularly occurs. However, the direct hyperpycnal river flow extinguishes itself very close to the Yellow River mouth, and most of the sediment is initially trapped within near-shore areas (Bornhold et al., 1986; Wright et al., 1990). Based on revised sediment gravity flow theory, Wright et al., (2001) reanalyzed field data collected offshore of the Yellow River in the 1980s and concluded that the turbid flows maintained by tidal currents could potentially move sediment downslope during slack tide when eddy viscosity temporally decreased.

Sediment gravity flows can be wave-supported (e.g., off the Po and Eel) or current-supported (e.g., off the Yellow River) based on the main source of turbulence. Wave-supported gravity flows have been well studied in the last decade, in part because they were observed in both the STRATFORM and EuroSTATAFORM projects, and also because bottom orbital velocities can be easily estimated from widely available surface wave parameters. Wave-induced flows are supported by velocity shear associated with wave orbital velocity within the thin wave boundary layer. Reduced shear at the top of the layer restricts the suspension from diffusing upward, potentially leading to very high sediment concentrations. Fluid mud with

78 sediment concentrations as high as 80 kg/m^3 were inferred within the wave boundary
79 layer on the Eel shelf (Traykovski et al., 2000; Wright et al. 2001). The capacity of
80 such flows to hold suspended sediment is limited by a balance between velocity shear
81 and sediment induced stratification as scaled by the Richardson Number (Wright et al.,
82 1999; 2001). Deposition from these flows is then determined by the gradient of
83 near-bed orbital velocity with depth (Traykovski et al., 2000; Scully et al., 2002) and
84 by depth-dependent changes in bed slope (Friedrichs and Scully, 2007).

85 Additional evidence of current-supported sediment gravity flows offshore of a
86 high-load river has been documented recently. Tripod observations collected on the
87 Waiapu mid-shelf, New Zealand (Fig. 1), in 2004 provided the first clear indication
88 that gravity flows supported by wind-driven mean currents could be an important
89 mode of across-shelf sediment dispersal (Ma et al., 2008). In contrast to thin (< 10 cm)
90 and dense (concentration ~10-100 kg/m^3) wave-supported gravity flows, the
91 current-supported gravity flows observed on the Waiapu shelf were significantly
92 diluted (depth-averaged concentration ~ 4 kg/m^3), and extended over a thicker layer
93 of 1~2 m (Ma, 2009). Compared with wave orbital velocities (based on wave buoys or
94 wave hindcasts), near-bed sub-tidal currents are often less predictable. As a result,
95 predicting the locus of deposition caused by current-supported gravity flow has
96 presented additional challenges (Wright and Friedrichs, 2006).

97 The Waiapu shelf is the first site to date where sediment gravity flows
98 supported by wind-driven currents have been documented (Ma et al., 2008). Such
99 flows are likely to be recognized in the future on many other energetic shelves. To

100 better understand the ramifications of such flows, this paper applies a
101 two-dimensional model for wave- and current-supported sediment gravity-driven
102 flows to the Waiapu River shelf. The main objectives of the paper are (i) to determine
103 whether sediment gravity flows may play a key role in forming the muddy deposits on
104 the Waiapu shelf during both low and high energy periods, (ii) to investigate the
105 effects of currents versus waves on gravity flows and resulting shelf deposition, and
106 (iii) to better understand the relative roles of local water depth and spatially varying
107 bed slope in determining the location of depocenters formed by gravity flows.
108

109 **2. Site description**

110 The Waiapu River drains a small mountainous basin (~1700 km^2),
111 characterized by steep terrain, heavy rainfall (~2.4 m/yr), unconsolidated soft Tertiary
112 mudstone and siltstone, and historical deforestation. As a result, its sediment yield
113 (~20,000 T km^2/yr) is among the highest in the world (Milliman and Syvistki, 1992).
114 Its water discharge is episodic over both inter- and intra-annual timescales, and almost
115 all of the discharge is associated with floods brought on by cyclonic storms.
116 Hyperpycnal plumes may occur in the Waiapu system during flood periods, i.e., total
117 suspended solids in the river can exceed 40 kg/m^3 (Mulder and Syvitski, 1995). At the
118 river mouth, fine-grained materials (>90%) dominate the sediment load (Hicks et al.,
119 2000).

120 Due to the small drainage basin of the Waiapu River, the river-ocean system is
121 strongly coupled in that the weather systems that produce heavy rains and river flows

122 also create energetic waves and wind-driven currents in the coastal ocean (c.f.
123 Wheatcroft, 2000). Bottom tripods deployed on the middle shelf (40-60 m) off the
124 Waiapu in 2004 indicated that significant wave height reached 3.5-5 m during storms
125 (Ma et al., 2008). In addition, currents at the tripod sites were observed to be strong,
126 exceeding 1 m/s at the surface and reaching 0.5 m/s near the seabed. Large-scale
127 circulations influence the outer shelf, including the southwestward East Cape Current
128 and northeastward Wairarapa Coastal Current (Chiswell, 2000).

129 The mid-to-outer continental shelf off the Waiapu River mouth is composed of
130 Holocene sediment that is locally over 100 m thick (Orpin et al., 2002), sitting atop up
131 to 1 km of Pleistocene sediments (Lewis et al., 2004). On the Waiapu inner shelf
132 thinner Holocene facies exhibit significant spatial variation, with river-plume and
133 event deposits dominating north and south of the river mouth, respectively (Wadman
134 and McNinch, 2008). On the mid-to-outer shelf the average modern accumulation rate
135 is about 1.5 cm/yr, with the highest accumulation rate at the Holocene depocenter of
136 about 3.5 cm/yr (Kniskern et al., 2009). Event layers have been found in the sediment
137 cores collected on the shelf break at the head of the Ruatoria Indentation, suggesting
138 the Ruatoria Indentation is a potential conduit through which sediment may escape to
139 deeper water (Kniskern et al., 2009).

140 Kniskern (2007) and Kniskern et al. (2009) measured the ^{7}Be and ^{210}Pb excess
141 activities of sediment cores collected throughout the Waiapu shelf in August 2003 and
142 May 2004. The half-life of ^{7}Be and ^{210}Pb are 53 days and 22 years, respectively,
143 hence they are used to infer deposition on the separate time scales of months and

144 decades. Figure 2 displays the ^{7}Be activities measured in surface sediment in May
145 2004 (Fig. 2a), just before the tripod deployment of Ma et al. (2008), and the
146 long-term accumulation rate based on excess ^{210}Pb profiles (Fig. 2b). The short-term
147 accumulation rate just before May 2004 was highest on the inner shelf (<50 m water
148 depth) but became close to zero on the middle-to-outer shelf, whereas the long-term
149 accumulation trend was reversed in that ^{210}Pb was mainly found seaward of 50 m. The
150 results indicated that rapid deposition occurred adjacent to the Waiapu River mouth in
151 the months leading up to May 2004, but most sediment probably moved seaward
152 across the shelf over longer time scales. Based on X-radiographs of the sediment
153 cores, Kniskern et al. (2009) concluded that long-term sedimentation on the Waiapu
154 shelf was by event deposits related to hyperpycnal flows.
155
156 **3. Theoretical development**
157 *3.1 Governing equations*
158 Integrated vertically over a sediment gravity flow layer, the momentum
159 balance can be represented as a downslope pressure gradient force induced by
160 suspended sediment opposed by an upslope frictional drag (Wright et al., 2001),

161 $$B\sin\alpha = C_D|u_{\max}|u_g. \qquad (1)$$

162 In Eq. (1) α ($\approx \sin\alpha \approx \tan\alpha$ for small α in radian units) is the seabed slope, C_D
163 is the frictional drag coefficient (~0.003), and u_g is the depth-averaged velocity of
164 the gravity-driven flow. The quantity $u_{\max}$ is the magnitude of the instantaneous
165 velocity at the top of the gravity layer, which can be expressed approximately as

$$u_{\max} = \sqrt{u_w^{\,2} + v_c^{\,2} + u_g^{\,2}}\,, \tag{2}$$

where u_w is the root-mean-square (r.m.s.) amplitude of wave orbital velocity (equal to $2^{1/2}$ times the standard deviation of the instantaneous orbital velocity), u_g is the downslope directed, gravity-driven current speed, and v_c is the speed of the non-gravity driven ambient current, mainly directed along-shelf. The depth-integrated buoyancy anomaly (B) induced by suspended sediment with mass concentration c_s can be estimated as

$$B = \rho_s^{\,-1} g s \int_{Z=0}^{\delta} c_s \, dz\,, \tag{3}$$

in which g is the acceleration of gravity, $s = (\rho_s - \rho_w)/\rho_w$ is the submerged weight of the sediment relative to seawater, ρ_s and ρ_w are the density of the sediment and water, and δ is the turbid layer thickness.

A key scaling parameter that controls the capacity of the gravity flow to hold suspended sediment is in the form of a Richardson number (Wright et al., 2001),

$$Ri = B / u_{\max}^{\,2}\,. \tag{4}$$

It expresses the importance of the stabilizing effects caused by stratification relative to the destabilizing effects induced by velocity shear. Bed stresses induced by intense waves and currents can generate strong bottom turbulence and can also resuspend bottom sediment causing strong stratification. The suppression of turbulence by stratification leads to settling of suspended sediment; but settling out of sediment then reduces stratification, which enhances turbulence once more. This negative feedback keeps Ri in the neighborhood of a critical value (of order $Ri \approx 1/4$), as has been demonstrated by field observations of bottom turbid layers on the Amazon shelf

188 (Trowbridge and Kineke, 1994), Eel shelf (Wright et al., 1999), and Waiapu shelf (Ma
189 et al., 2008).

190 Combining Eqs. (1), (3), and (4) yields the following expressions for u_g and
191 for the depth-integrated sediment concentration for periods when the turbid layer has
192 reached its maximum sediment capacity:

193 $$u_g = \beta \cdot u_{\max} = \beta \cdot \sqrt{\frac{u_w^{\,2} + v_c^{\,2}}{1-\beta^2}} \quad , \tag{5}$$

194 $$\int c_s dz = \frac{Ri_{cr}\rho_s}{gs}\left[\frac{u_w^{\,2} + v_c^{\,2}}{1-\beta^2}\right], \tag{6}$$

195 where $\beta = Ri_{cr}\alpha / C_D$. Thus the maximum downslope rate of sediment transported by
196 gravity flows can be estimated by as the product of Eqs. (5) and (6):

197 $$Q_g = u_g \int c_s dz = \frac{\rho_s Ri_{cr}^{\,2}\alpha}{gsC_D}\left(\frac{u_w^{\,2} + v_c^{\,2}}{1-\beta^2}\right)^{3/2}. \tag{7}$$

198 The rate of downslope sediment transport increases with bed slope, α, as well as
199 with the magnitude of wave orbital velocity, u_w, and with the near-bed ambient
200 current speed, v_c. Note that we require $\beta < 1$ for wave- and/or current-supported
201 gravity flows to exist. If $\beta \geq 1$ (i.e., $\alpha \geq C_D/Ri_{cr} \approx 0.012$), the shelf becomes
202 sufficiently steep for gravity flows to become autosuspending (Wright et al., 2001).

203

204 *3.2 Gravity-induced deposition*

205 The rate of deposition is determined by spatial convergence in sediment
206 transport, which is simplified mathematically if one defines *x* as being directed along
207 the downslope streamline being followed by Q_g. Then

208 $$D = -\nabla \bullet \vec{Q}_g = -\frac{\partial Q_g}{\partial x} - \frac{Q_g}{R}, \quad (8)$$

209 where R is the radius of curvature of the local bathymetric contour. Eq. (8) highlights
210 two distinct transport patterns affecting deposition, one due to gradients in the
211 downslope rate of sediment transport ($\partial Q_g/\partial x$), and one due to lateral convergence or
212 divergence of transport streamlines associated with plan-view curvature of isobaths
213 (Q_g/R). If the bathymetric contours are lobate ($R > 0$), then deposition is reduced; if
214 the contours are embayed ($R < 0$), then deposition is increased.

215 In calculating $\partial Q_g/\partial x$ (using the expression for Q_g from in Eq. (7)), it is
216 reasonable to assume that gradients in u_w^2 dominate gradients in v_c^2, since ambient
217 mean currents (v_c) typically decay with water depth much more slowly than bottom
218 wave orbital velocity (u_w). Thus deposition by sediment gravity flows can be
219 approximately re-expressed as:

220 $$D = Q_g \{-\frac{3u_w}{u_w^2 + v_c^2}\frac{\partial u_w}{\partial x} - \frac{1+2\beta^2}{(1-\beta^2)\alpha}\frac{\partial \alpha}{\partial x} - \frac{1}{R}\}. \quad (9)$$

221 Eqs. (7) and (9) together show that when $Ri = Ri_{cr}$, the deposition rate is controlled by
222 the near-bed wave orbital velocity amplitude (u_w), near-bed ambient current speed (v_c),
223 and shelf slope (α). Since wave orbital velocity attenuates strongly with water depth,
224 the first term in the brackets on the right hand side (r.h.s.) of (9) always favors
225 deposition. The second term in the brackets either increases deposition if the
226 across-shelf bathymetric profile is concave upward ($\partial\alpha/\partial x < 0$), or decreases
227 deposition if the profile is convex upward ($\partial\alpha/\partial x > 0$). The third term accounts for
228 lateral convergence or divergence.

For wave-dominated conditions over a linearly (or nearly linearly) sloping bed along a relatively straight coastline, i.e., $|\partial u_w/\partial x|$ large with $|\partial\alpha/\partial x|$ and $|1/R|$ small, the first term on the r.h.s. of Eq. (9) will dominate. This is the case to lowest order for the mid-shelf depocenter off the Eel River, where deposition occurs mainly due to u_w decreasing with greater depth (Traykovski et al. 2000; Scully et al. 2002). But if bed slope rapidly decreases with distance offshore, producing a strongly negative $\partial\alpha/\partial x$, then deposition from a wave-supported gravity flow may be dominated instead by changes in bed slope via the second term on the r.h.s. of Eq. (9). This is case off the Po River, where the depocenter is near the roll-over point on the profile the subaqueous delta, i.e., near the point of the most strongly negative $\partial\alpha/\partial x$ (Friedrichs and Scully, 2007).

Assuming that the depth-dependence of v_c is small, the sensitivity of sediment deposition to spatial variations in bed slope ($\partial\alpha/\partial x$) increases dramatically for current-supported gravity flows in the absence of waves. For the hypothetical case of $v_c >> u_w$, Eq. (9) reduces to

$$D = \frac{\rho_s R i_{cr}^{\ 2} \alpha\ v_c^{\ 3}}{gsC_D(1-\beta^2)^{3/2}}\left\{-\frac{(1+2\beta^2)}{(1-\beta^2)\alpha}\frac{\partial\alpha}{\partial x}-\frac{1}{R}\right\}. \qquad (10)$$

We see from Eq. (10) that current-supported gravity flow deposition is not dependent on absolute depth, and, therefore, deposition due to spatially uniform currents can occur deeper than that due to waves. Keeping in mind that β is proportional to bed slope (α), deposition by current-supported flows will occur where $\partial\alpha/\partial x$ is negative and α is relatively large (as long as β remains less than 1). This optimal combination of negative $\partial\alpha/\partial x$ and large α is likely to occur just downslope of the locations where

bed slope first begins to decrease with depth, i.e., just downslope of regions of maximum α. Current-induced deposition will be further enhanced where bathymetry is embayed (i.e., where $R < 0$).

4. The two-dimensional model

4.1 Model implementation

The two-dimensional implementation of Eqs. (1) – (8) was developed by Scully et al. (2003) and has been applied successfully on the Eel (Scully et al., 2003) and Po (Friedrichs and Scully, 2007) shelves to represent patterns of muddy flood deposit formation in response to wave-supported gravity flows. In this paper we extend the two-dimensional model to include the effect of significant ambient currents by retaining a spatially uniform but temporally varying value for v_c in Eq. (2). When there is sufficient river-delivered sediment available to allow $Ri=Ri_{cr}$, the model solves the aforementioned equations in rectangular coordinates to predict the maximum possible gravity flow velocity and rate of sediment deposition. If insufficient sediment is available and u_{max} exceeds a threshold value (u_{erode}), previously deposited sediment is eroded from the bed until $Ri=Ri_{cr}$. If sufficient sediment is still unavailable, subcritical gravity flows move downslope according to Eq. (1) without depositing sediment (Scully et al., 2003). For all of the model runs presented in this paper, Ri_{cr} = 1/4, C_d = 0.003 and u_{erode} = 0.35 m/s, the same values used for the Po shelf by Friedrichs and Scully (2007).

For the present application, the active model domain covered a region extending along-shore from 11 km northeast of the Waiapu River mouth to 19 km southwest of the river mouth, and from the coastline to offshore near the 170-m isobath of the Ruatoria Indentation (Fig. 1). The domain was composed of 145×127 rectangular element grids, and each grid cell represented an area of about 207 m in the along-shelf direction and 193 m in the across-shelf direction. Unsmoothed bathymetry, which is shown in Figure 1, was provided by NIWA (New Zealand National Institute of Water & Atmospheric Research). The shorelines were digitized from a world coastlines database (http://www.ngdc.noaa.gov/mgg/shorelines/shorelines.html), and the water depth along the shoreline was assigned to be zero. Bathymetry was then smoothed in both the along- and across-shelf directions first via a two-dimensional triangle filter and then by a cubic spline on every seventh grid point. Finally, the shelf slopes in the along- and across-shelf directions were calculated based on the smoothed bathymetry.

The two-dimensional model was applied to the Waiapu shelf for the 12-month period extending from 1 September 2003 to 31 August 2004. This period was chosen to cover both storm and calm weather seasons, to encompass the observations of sediment accumulation collected by Kniskern (2007) and Kniskern et al. (2009), and to overlap the tripod observations reported by Ma et al. (2008). Wave period and height, shelf current speed, and riverine sediment discharge were the required time-varying model inputs. Since the simulation period was longer than the available tripod observations, hindcast data for wave height, wave period, and wind velocity

294 were derived from the NOAA WAVEWATCH-III global ocean wave model
295 (NWW3). NWW3 is a publicly available, third generation global wave model with a
296 resolution of 1.25^0 longitude and 1^0 latitude (Tolman, 2002). NWW3 wave heights
297 then were calibrated based on wave heights inferred from tripod observations by Ma
298 et al. (2008), and NWW3 winds were related to the observed along-shelf currents. The
299 most reliable tripod data were from May to July 2004; the observed waves and
300 currents were all obtained within this time interval from an Acoustic Doppler
301 Velocimeter (ADV) mounted about 40 cm above the seabed on the tripod at the 60-m
302 isobath (see Fig. 1).
303
304 *4.2 Wave input*
305 Although the NWW3 grid spacing (1.25 by 1 deg) is relatively coarse, the
306 nearest NWW3 node is advantageously located, only 30 km offshore of the Waiapu
307 River mouth (Fig. 1). The NWW3 hindcast reported significant wave height (H_{sig}),
308 whereas the two-dimensional model used r.m.s. wave height ($H_{rms} = H_{sig}/2^{1/2}$). To
309 correct for this and also help compensate for other potential systematic differences,
310 the NWW3 wave heights were multiplied by a constant such that the 90^{th} percentile of
311 all NWW3 wave heights reported from May to July 2004 equaled the 90^{th} percentile
312 of all H_{rms} values (H_{rms90}) observed at the 60-m tripod site (Fig. 3a). H_{rms90} was found
313 by Friedrichs and Wright (2004) to be an appropriate statistic for predicting
314 wave-supported gravity flows offshore of a variety of rivers around the globe. A

315 reasonably strong correspondence was found between observed waves at the tripod
316 and the calibrated NWW3 hindcast with a correlation coefficient of 0.76 (Fig. 3a).
317 Efforts were made to relate NWW3 hindcast wave periods to those observed at
318 the tripod, but no conclusive relationship was found (the correlation was only 0.06).
319 Other researchers (Trembanis et al. 2007) have similarly found that comparisons
320 between NNW3 hindcasts and observations were much better for wave height than for
321 wave period. Following Friedrichs and Wright (2004), we instead estimated wave
322 periods as a function of wave height for the NWW3 hindcast by assuming

323 $$T = C \cdot \sqrt{H_{rms}}\,, \qquad (11)$$

324 in which C is a dimensional constant. Assuming the most reliable observations of
325 wave period from our tripod data were from when waves were large (observed T = 12
326 s when H_{rms} = 2.5 m, see Ma et al., 2008), we used C = 7.6 s m$^{-1/2}$. Time-varying r.m.s.
327 near-bed orbital velocity amplitude was then predicted throughout the model domain
328 using a spatially uniform wave height (from the calibrated NWW3 hindcast of H_{rms}),
329 spatially uniform wave period (from Eq. (11)), spatially varying local water depth
330 (from the smoothed bathymetry), and linear wave theory.
331
332 *4.3 Current input*
333 During storms, tidally-averaged currents on the Waiapu shelf were often
334 stronger than wave orbital velocities (Ma et al., 2008). In contrast to the Eel and Po
335 cases, where waves were assumed to dominate during storms, ambient mean currents
336 on the Waiapu shelf could not be neglected in the calculation of u_{max} (see Eq. 2). If

337 one assumes that the along-shelf current (v_c) dominates the across-shelf current, and
338 that v_c is predominantly driven by the along-shelf wind stress, it follows that

339 $$v_c \sim [v_{wind} \times (u_{wind}{}^2 + v_{wind}{}^2)^{1/2}]^{1/2}, \quad (12)$$

340 where v_{wind} and u_{wind} are the along- and across-shelf wind speed. The correlation
341 between the observed along-shelf current and the right-hand-side of Eq. (12) using
342 NWW3 hindcast winds for May to July 2004 was a reasonably strong 0.70.

343 Given this encouraging relationship, the NWW3 winds were converted to
344 along-shelf currents based on a linear regression against Eq. (12), and then the result
345 was multiplied by a constant to ensure that the hindcast currents had the same energy
346 (i.e., sum of the squared current velocities) as the observed v_c (Fig. 3b). Finally, the
347 time-series for along-shelf current velocity was assigned uniformly onto each model
348 grid point without considering energy decay with water depth or possible topographic
349 effects. Note that in the simulations considered here, ambient currents contributed to
350 the carrying capacity of sediment gravity flows, but ambient currents did not advect
351 sediment.

352

353 *4.4 Sediment input*

354 The model assumed that no pre-existing erodible sediment was available on
355 the seabed at the beginning of each model run and that the only source of sediment
356 input was fine-grained material delivered by the river. The sediment discharge
357 time-series for the Waiapu River was provided by NIWA and was calculated by
358 applying the Waiapu rating curve from Hicks et al. (2004) to the water discharge

359 measured by the Gisborne District Council. However, the sediment input to the
360 gravity flow model was set to be only 23% of the amount predicted by the rating
361 curve, based on the sediment budget of Kniskern et al (2009). Using ^{210}Pb
362 accumulation rates for the Waiapu shelf between 40-m and 200-m water depth,
363 Kniskern et al. (2009) could account for just 23% of the sediment discharge predicted
364 by Hicks et al. (2004).

365 Sensible reasons for reducing the fraction of the total sediment load available
366 for gravity flows include the following: (i) The rating curve includes sands, while
367 only fine sediment is transported by the modeled gravity flows. (ii) According to
368 Hicks et al. (2004), the rating curve contains inherent uncertainty on the order of 40%
369 and may overestimate the sediment concentration at high discharge because of the
370 weighting given to concentrations associated with a few very high concentration,
371 extremely high-yield events. (iii) The river gauging station is 20 km upstream from
372 the river mouth. Because of river channel aggradation, the amount of sediment
373 delivered to the Waiapu coastal ocean is likely less than that inferred 20 km upstream.
374 (iv) Some portion of the fine sediment exiting the Waiapu is likely to remain
375 unflocculated, reducing the likelihood of it initially settling near the river mouth. (v)
376 Riverine sediment are dispersed over the Waiapu shelf not only by gravity-driven
377 flow, but also by other mechanisms, such as classical wave-current resuspension,
378 which likely carries significant amount of sediment out of the model domain
379 (Kniskern et al., 2009). (vi) In their application of the two-dimensional gravity flow
380 model to the Po shelf, Friedrichs and Scully (2007) also reduced riverine sediment

input to a fraction of that predicted by the Po rating curve (56% in their case) for analogous reasons.

Sediment was introduced into the model along the coast as a line source. Two distinct line sources were considered, a base case which decreased sediment input linearly both north and south of the river mouth (Fig. 4), and a second case with spatially uniform input all along the model's landward edge. The southern and northern limits of sediment input (and the extent of the model domain) were set to coincide with coastal promontories that are likely to form a natural littoral cell. The methodology here was again consistent with the approach of Friedrichs and Scully (2007), who examined both spatially uniform and spatially varying line sources off the Po. Based on the bulk density of cores reported by Kniskern et al. (2009), a seabed porosity of 0.6 was used here to estimate the ultimate deposit thickness.

4.5 Low and high energy periods

A year-long time-series of waves and currents was generated by applying the methods discussed above to the available NWW3 hindcast. The estimated r.m.s. wave height and along-shelf current velocity from September 2003 to August 2004 are shown in Figures 5a and 5b, based on which the 12-month period can be divided into two portions: 1) a low-energy period (LEP) from early September 2003 to the mid-May 2004, and 2) a high-energy period (HEP) from mid-May to late August 2004. During the LEP, mean r.m.s. wave height and current speed were 0.8 m and 0.08 m/s, respectively, and only one significant sediment-yield event occurred (Fig.

403 5c). During the HEP, r.m.s. wave height and current speed were 1.3 m and 0.12 m/s
404 on average. Several high discharge events occurred during the HEP, providing
405 abundant sediment to feed gravity-driven flows (Fig. 5c).

406 Given the r.m.s. wave heights in Figure 5a, the ambient currents in Figure 5b,
407 and the relation for wave period given by Eq. (11), it is straightforward to apply linear
408 wave theory to solve for the time-series of depths at which the strength of the ambient
409 mean current, v_c, first exceeded the r.m.s. amplitude of wave orbital velocity, u_w.
410 Since the strength of the total sediment gravity flow velocity is a simple function of
411 $u_w^2 + v_c^2$ (see Eq. 5), it follows that this depth was also approximately the point at
412 which current-supported gravity flows first dominated wave-supported gravity flows.
413 Figure 5d displays daily median values for this cross-over depth. During energetic
414 periods, u_w commonly exceeded v_c down to about 60-m depth. The median depth at
415 which v_c first exceeded u_w for all times with H_{rms} greater than 2 m in height was h =
416 61.8 m.

417

418 **5. Base Case Results**

419 *5.1 Predicted versus observed gravity flow velocities*

420 With the wave orbital velocity, current speed, and bed slopes known at each
421 grid point, the two-dimensional model solved for across-shelf gravity flow velocity
422 (u_g) as described in Section 4. Modeled u_g at the grid point nearest to the 60-m tripod
423 site in response to calibrated NWW3 forcing was compared with observed u_g in Fig. 6
424 (using observations from Ma 2009). The observed u_g was defined as the near-bed

425 across-shelf velocity from the second bin of the downward-looking Pulse Coherent
426 Acoustic Doppler Profiler (~ 43 cm above the bed) minus the free stream across-shelf
427 velocity from the middle bin of the upward-looking Acoustic Doppler Current Profiler
428 (~ 26 m above the bed) for the period of May to July 2004, when the most reliable
429 tripod data were available.

430 The order of magnitude and frequency of the observed and modeled u_g time
431 series match well (Fig. 6), which is key for successfully reproducing the general
432 nature of the observed sediment deposits during the low- and high-energy hindcasts.
433 The fine-scale time lags between the details of the observed u_g time series and the
434 model calculations forced by NWW3 reflect some discrepancy between the actual
435 ambient waves and currents and those inferred from NWW3 time series.

436

437 *5.2 Deposition during low-energy period*

438 The low-energy portion of the NWW3 hindcast covered 257 days, about 5
439 times the half-life of ^{7}Be. This period was divided into 10 segments, and at the end of
440 each segment the modeled deposit thickness was multiplied by a decay factor so that

441 $$D_{j+1} = D_j \cdot e^{-\Delta t / t_{1/2}}, \quad (13)$$

442 where D_j is the deposit thickness predicted at the end of segment j, D_{j+1} is the deposit
443 thickness saved for the next segment $j+1$, Δt is 25.7 days, and $t_{1/2}$ is the half-life of
444 ^{7}Be (53.3 days). In this way, the final deposit was weighted toward more recent
445 deposition in order to roughly represent the fraction of sediment potentially tagged

446 with actively decaying ^{7}Be. Finally, the LEP deposit thickness was normalized by its
447 maximum thickness to represent relative ^{7}Be activity on a scale of 0 to 1.

448 Figure 7 displays the predicted ^{7}Be distribution for the LEP. The modeled high
449 activity sediment was almost entirely deposited at water depths shallower than 80 m,
450 with the maximum activity found along the 40-to-50-m isobath. The focusing of the
451 deposit along the 50-m isobath, at least in the region of the tripods, was likely in
452 response to a local maximum in bed slope just landward of that depth (Fig. 8). As
453 discussed in Section 3.2, greatest deposition by sediment gravity flows under low
454 wave conditions tends to occur where steep slopes first stop increasing with distance
455 offshore. This is because a downslope-directed decrease in bed slope favors sediment
456 flux convergence. Deposition during the LEP was generally closer to shore than
457 during the HEP because the depth-dependent wave orbital velocities were small, and
458 even a relatively low sediment supply overwhelmed the wave-supported gravity flow
459 capacity in relatively shallow water.

460 Pockets of high activity deposition during the LEP were somewhat patchy,
461 most likely in response to remaining local irregularities in the smoothed bed slope.
462 This is consistent with the results from Kniskern et al. (2009) who examined the
463 penetration depths of Kasten cores and found that muddy sediment deposits landward
464 of the 80-m isobath were patchy. Deposition south of river mouth in particular may
465 have been concentrated by a subtle bathymetric trough that extends southward from
466 the river mouth near the coast and becomes indistinct toward the mid-shelf (Wadman

467 and McNinch, 2008). Gravity flows are expected to move sediment along the trough,
468 following the local bathymetry (Wadman and McNinch, 2008).

469 The markers (stars, crosses, triangles) superimposed on the predicted LEP
470 deposition (Fig. 7) indicate sites of observed non-zero ^{7}Be activities from within the
471 model domain based on the May 2004 survey of Kniskern (2007). The highest
472 observed ^{7}Be activity (shown as stars) generally matched modeled areas of high
473 activity, while medium (crosses) and relative lower activities (triangles) surrounded
474 the isolated depocenters. Both the model results and observations showed that in the
475 short-term (~ 5 months), sediment delivered by the Waiapu River during periods of
476 low energy was mainly trapped between the 20- and 80-m isobaths.

477

478 *5.3 Deposition during high-energy period*

479 The result of the 2-D model calculation for the high-energy period (HEP) is
480 displayed in Figure 9. The main HEP depocenter was elongated and occurred
481 southeast of the river mouth, between 60- and 120-m water depths, trending offshore
482 toward the north, oblique to the shelf bathymetric contours. Its locus (Fig. 9) matched
483 remarkably with that of the observed highest long-term accumulation rate as shown in
484 Figure 2b. Across- and along-shelf profiles of deposition for the HEP base case are
485 shown by solid lines in Figures 10a and 10b. The maximum accumulation calculated
486 by the model for the outer shelf depocenter was about 5 cm (Fig .10a), roughly
487 consistent with the maximum observed long-term accumulation rate of 3.5 cm/yr. In
488 contrast, the HEP base case predicted as much as 10 cm of deposition 8 km southwest

of the river mouth (Fig. 10b), over-predicting the long-term observed annual deposition by more than a factor of two. However, Kniskern et al. (2009) also documented the presence of individual, rapidly emplaced flood layers up to 20 cm thick. Local disagreement between observed and modeled thickness could be the result of several factors, with likely candidates including errors in the assumed distribution of riverine sediment input, non-gravity flow resuspension and transport, and localized errors in model bathymetry.

The location of the obliquely trending depocenter was just downslope of a likewise obliquely trending maximum in bed slope (Fig. 8). Thus deposition on the Waiapu shelf during the HEP was accentuated where bed slope first started decreasing offshore in a manner consistent with that suggested by the $\partial\alpha/\partial x$ term in Eq. (10). During the HEP there was also a tendency for a secondary depocenter to form along the 65-to-70-m depth contour (Fig. 9), presumably just offshore of the point where u_{max} could no longer transport all the available riverine sediment. Thus the mechanism which formed this secondary line of deposition is consistent with the behavior suggested by the $\partial u_w/\partial x$ term in Eq. (9). The line of first deposition was deeper during the HEP than during the LEP because of the greater transport capacity of the more energetic wave orbitals. Finally, the $1/R$ term in Eqs. (9) and (10) also helps explain enhanced deposition at ~70-m and ~120-m depths at the southwest and northeast ends of the main depocenter. Both these areas of concentrated deposition occurred where the bathymetric contours are embayed, favoring lateral transport convergence.

510 During the HEP simulation, of the 7.5 MT of sediment included in the gravity
511 flow model, about 88% was deposited within the model domain; 10% escaped into the
512 deep sea; 2% went northward out of the model domain; and less than 1% went
513 southward out of the domain. Although this model could not evaluate the fate of
514 sediment that was not associated with gravity flows, model results clearly suggested
515 that it was during high-energy periods that the sediment delivered by the Waiapu
516 River was transported by gravity-driven flows into the long-term shelf depocenter
517 identified by Kniskern et al. (2009).
518
519 **6. Model sensitivity**
520 *6.1 Currents vs. waves*
521 As indicated by Eqs. (9) and (10), currents can compensate for the decay of
522 wave orbital velocity with depth and hence can cause sediment to accumulate farther
523 offshore and in deeper water. The sensitivity of sediment accumulation to
524 current-supported gravity currents was tested by running the 2-D model with and
525 without v_c. Solid and dashed lines in Figures 10(a) and 10(b) display predicted
526 sediment deposition profiles with and without current-supported gravity flows. The
527 across-shelf profile (Fig. 10a) passes through the tripod sites and the northern end of
528 the primary and secondary depocenters in Figure 9. The along-shelf profile Fig. 10b)
529 roughly parallels the 70-m isobath, cutting through the southwest portion of the main
530 depocenter.

With strong currents, the location of greatest deposition was centered around 115 m, with secondary deposition near 65 m (solid line in Fig. 10a). The deeper depocenter, favored more by current-induced deposition, occurred just offshore of a local maximum in bed slope (α) (Fig. 10e), in a region of where α was decreasing offshore (Fig. 10g). This association of current-induced deposition with $\partial\alpha/\partial x < 0$ is consistent with the arguments presented in Section 5.3. Without currents, however, much more sediment was deposited near 65-m depth (dashed line in Fig. 10a), where the decay of wave orbital velocities with depth caused wave-supported gravity currents to first lose their capacity to carry all of the available riverine sediment. Deposition by wave-supported gravity flows is relatively more sensitive to total depth, while deposition by current-supported gravity flows is relatively more sensitive to seabed slope. This is why the wave-induced deposit more closely paralleled the bathymetry (following a pattern in h), while the current-influenced deposit cut diagonally crossed the bathymetry (following a pattern in α).

For the waves only case, the general trend of the along-shelf distribution of deposition (dashed line in Fig. 10b) more closely followed the along-shelf distribution of riverine sediment input (see Fig. 5). In contrast, the along-shelf distribution of deposition for the current-influenced case at ~70-m depth was strongly shifted to the south of the river mouth (solid line in Fig. 10b). This difference can be understood in part by examining the along-shelf distribution of the change in slope with depth (Fig. 10h). At 70-m depth north of the river mouth, $\partial\alpha/\partial x$ is positive, whereas at this depth south of the river mouth $\partial\alpha/\partial x$ is generally negative (Fig. 10h). Since $\partial\alpha/\partial x \geq 0$

553 favors bypassing by current-supported gravity currents and $\partial\alpha/\partial x < 0$ favors
554 deposition, the current-influenced case at this depth (solid line) has deposition focused
555 to the south. The wave-only case (dashed line) is more sensitive to absolute depth
556 than to changing bed slope, so deposition at 70 m more-or-less mimics the distribution
557 of sediment supply. However there is still a slight displacement of the wave-only case
558 to the south, suggesting at least a minor sensitivity of wave-induced deposition to bed
559 slope.
560
561 *6.2 Along-shelf curvature of isobaths*
562 Another factor that shifts the along-shelf pattern of deposition away from
563 mirroring the distribution of riverine input is along-shelf curvature of isobaths, i.e.,
564 bathymetry with a finite radius of curvature (see Eqs. 8-10). Unlike the influence of
565 the across-shelf profile, along-shelf curvature of isobaths can lead to lateral flux
566 convergence or divergence. One way to evaluate the effect of curving bathymetry is to
567 examine the component of bed slope along our along-shelf transect (Fig. 10f). From
568 the southern end of the along-shelf transect to about 6 km south of the river mouth,
569 the along-transect slope component tends to decrease overall (i.e., $1/R < 0$), favoring
570 gravity flow convergence. In other words, isobaths in that region are generally
571 embayed (see Fig. 9). But from that point northward in Figure 10f, the along-transect
572 slope at 70-m depth increases (the contours are lobate with $1/R > 0$), favoring gravity
573 flow divergence. (Note that at ~115 m, at the site of the offshore depocenter, the
574 contours are embayed once more, favoring convergence – see Fig. 9).

575 The sensitivity of sediment accumulation to the curvature of isobaths was
576 explicitly tested by re-running the 2-D model for the HEP base case, but with the bed
577 slope in the along-shelf component of the model's rectangular grid set to zero
578 (dot-dashed line in Figs. 10a and 10b). With the bed slope in the direction of the
579 along-shelf transect turned off, the across-shelf distribution of deposition was changed
580 notably in that more sediment was shifted to the shallower depocenter relative to the
581 deeper depocenter (Fig. 10a). This makes sense because the divergent effect of lobate
582 contours was no longer felt at 65 m, and the convergent effect of embayed contours
583 was no longer felt at 115 m. With the along-shelf bed slope set to zero, the along-shelf
584 shelf distribution of deposition at ~70 m was much smoother (Fig. 10b), indicating
585 that much of the patchiness in the base run was likely to do local divergence and
586 convergence associated with bathymetric curvature. In comparing Figures 10b and
587 10d it is clear that local changes in along-shelf slope are correlated to local changes in
588 deposit thickness.
589
590 *6.3 Along-shelf distribution of sediment input*
591 To test the sensitivity of model calculations to the along-shelf input of riverine
592 sediment, the 2-D model was also run using a line source that spread sediment input
593 equally along the coast with the same total sediment load as the base model run
594 (dashed line in Figs. 10c and 10d). Except for the region 10 to 15 km south of the
595 river mouth, the relative thickness and spatial distribution of the resulting deposit was
596 remarkably similar to the base case. This was an encouraging result, because the

597 original along-shelf distribution of riverine sediment input (see Fig. 5) was relatively
598 arbitrary and unconstrained by observations. The deposit resulting from a uniform line
599 source was proportionally thinner from 8 km south to 5 km north of the river mouth
600 because the uniform line source provided less riverine sediment than the base case in
601 that region. The only major change was between 11 and 16 km south of the river
602 mouth, where the locally increased riverine supply combined with embayed contours
603 led to a notably thicker deposit.

604 A key result was that even with uniform sediment input, the main depocenter
605 created by the current-influenced gravity flow model was still in the same general
606 location and was still oblique to the bathymetry, consistent with the observations of
607 Kniskern et al. (2009). This supported the conclusion that subtle aspects of shelf
608 bathymetry played a dominant role in controlling the location and shape of the
609 depocenter.

610

611 *6.4 Total sediment input*

612 The appropriate factor by which to adjust the sediment rating curve for the
613 base model run was weakly constrained. The base run adopted 23% of the total
614 predicted sediment delivery, mainly based on the sediment budget of Kniskern et al.
615 (2009) (see discussion in Section 4.4). To illustrate the impact of varying the total
616 amount of sediment input, another model run was conducted with double the original
617 amount of sediment and the same wave and current conditions as the base case.

With double the riverine sediment load, deposition increased proportionally more in shallow water than in deep water (Fig. 10c), because the depth at which the greater sediment supply overwhelmed the capacity of wave-supported gravity flows became shallower. Along the 70-m along-shelf profile, the thickness of the deposition more or less doubled (Fig. 10d), although the base-case peak in deposition 8 km southwest of the river mouth became less dominant. This is consistent with a greater role for wave-supported gravity currents at shallow depths (< ~80 m) as sediment load was increased. Current-supported gravity currents presumably remained dominant in deeper water, because the shelf-oblique mud deposit remained prominent.

Overall, doubling the sediment input relative to the base case caused the model to significantly overpredict the observed thickness sediment deposition on the Waiapu shelf. Nonetheless, the general spatial distribution of deposition remained almost the same. This provides a further support of our main conclusion that shelf bathymetry and associated bed slope strongly influenced the location and shape of the depocenter off the Waiapu River.

7. Summary and Conclusions

The Waiapu system provides a prototype for investigating the relative importance of wave- versus current-supported gravity flows on shelf deposition. Such flows are likely to be recognized in the future on many other energetic shelves. In this paper, the two-dimensional gravity-flow model developed by Scully et al. (2003) was applied to the Waiapu shelf by accounting for not only maintenance by waves but also

640 by wind-driven currents. The purpose was to evaluate the likely significance that
641 sediment gravity flows, especially current-supported flows, played in forming muddy
642 shelf deposits. Additional focus was placed on contrasting deposition during high
643 versus low energy periods and on better understanding the relative roles of local water
644 depth versus spatially varying bed slope in determining the location of the deposits.

645 The model and its interpretation was based on analytical theory for
646 critically-stratified gravity flows supported by ambient waves and currents as
647 described by Wright et al. (2001) and as further extended in this paper. Basic model
648 parameters, including the Richardson number (0.25), the bottom drag coefficient
649 (0.003), and the critical velocity for seabed erosion (0.35 m/s) were consistent with
650 those used previously for the Eel (Scully et al., 2003) and Po (Friedrichs and Scully,
651 2007) shelves. To account for support of gravity flows by wind-driven currents, winds
652 hindcast by the NOAA WAVEWATCH III were correlated to shelf current speed.
653 Tripod data collected at 60-m depth from May to July 2004 were used to calibrate the
654 WAVEWATCH III forcing, including wave heights and wind-induced along-shelf
655 currents.

656 The model successfully reproduced the main depositional features of the
657 riverine sediment on the Waiapu shelf by representing both the magnitude and
658 location of the observed muddy deposit. During the fair weather season from
659 September 2003 to May 2004, sediment tended to be trapped between the water
660 depths of 20 and 80 m, consistent with the distribution of ^{7}Be in May 2004 cores as
661 reported by Kniskern (2007). During the storm season in the months of May through

August 2004, riverine sediment was transported further offshore, because during this time stronger waves and currents had an increased capacity to carry sediment. The resulting shelf-oblique deposit was consistent with the long-term (100 yr) accumulation pattern as indicated by ^{210}Pb (Kniskern et al., 2009). Analytical theory and numerical results revealed that riverine sediment supply, marine forcing (waves and currents), and bathymetry (depth, slope and along-shelf curvature) were the key factors that influenced patterns of shelf deposition.

Currents and waves were shown to play distinct roles in sediment transport and distribution of resulting deposits. Currents tended to dominate the sediment gravity flows in water depths that exceeded about 60 m, where waves became secondary due to rapid decay of orbital velocities. Where waves dominated gravity-driven deposition, the deposits tended to occur at shallower water depths and parallel to the isobaths. This pattern occurred because transport convergence due to waves was driven by the strong dependence of near-bed orbital velocity on absolute depth. In contrast, current-supported gravity flows were not a function of absolute depth and thus could compensate for the decay of wave orbital velocity and move sediment further offshore. Instead, current-supported flows were highly sensitive to the slope of the seabed, and deposition by current-supported gravity currents occurred where bed slope decreased with distance offshore and where isobaths were embayed.

Sensitivity tests revealed the relative importance of the magnitude and along-shelf distribution of sediment input. The base case assumed 23% of the river's load was available for shelf deposition (based on the budget of Kniskern et al. 2009)

and that a maximum in sediment input occurred directly offshore of the river mouth. Doubling the sediment load or using a uniform along-shelf sediment distribution locally changed the deposit thickness, but the location and oblique trend of the mid- to outer-shelf depocenter remained similar to observations. The relatively insensitivity of the depocenter to sediment load was encouraging since the details of riverine input were poorly constrained.

Sediment transport across the Waiapu shelf resulted from a combination of both wave- and current-supported gravity flows. However, we conclude that the longer term (~100 yr), shelf-oblique mud deposit found between the 60- and 120-m isobaths mainly reflects current-supported gravity flows and their response to local variations in seabed slope and bathymetric curvature. Under high-energy conditions, wave-supported flows over the inner shelf transition to current-dominated support as the flows move progressively into deeper water.

Acknowledgments

Funding for this study was provided by the National Science Foundation Marine Geology and Geophysics Program (Grant OCE-0326831) and by the Office of Naval Research Coastal Geosciences Program (Grant N00014-04-0628). We thank M. Scully for his assistance in implementing the two-dimensional model code. We also thank T. Kniskern for helpful discussions regarding sediment accumulation processes on the Waiapu Shelf. This is contribution no. XXXX from the Virginia Institute of Marine Science.

728 **References**

729 Bornhold, B.D., Yang, Z.S., Keller, G.H., Prior, D.B., Wiseman, W.J., Wang, Q.,
730 Wright, L.D., Xu, W.D., Zhuang, Z.Y., 1986. Sedimentary framework of the
731 modern Huanghe (Yellow River) delta. Geo-Marine Letters 6, 77-83.
732 Chiswell, S.M., 2000. The Wairarapa coastal current. New Zealand Journal of Marine
733 and Freshwater Research 34, 303-315.
734 Friedrichs, C.T., Wright, L.D., 2004. Gravity-driven sediment transport on the
735 continental shelf: implications for equilibrium profiles near river mouths.
736 Coastal Engineering 51, 795-811.
737 Friedrichs, C.T., Scully, M.E., 2007. Modeling deposition by wave-supported gravity
738 flows on the Po River prodelta: from seasonal floods to prograding clinoforms.
739 Continental Shelf Research 27, 322-337.
740 Harris, C.K., Traykovski, P., Geyer, W.R., 2005. Flood dispersal and deposition by
741 near-bed gravitational sediment flows and oceanographic transport: A
742 numerical modeling study of the Eel River shelf, northern California. Journal
743 of Geophysical Research 110 (C9), 25-1 - 25-16.
744 Hicks, D.M., Gomez, B., Trustum, N. A., 2000. Erosion thresholds and suspended
745 sediment yields, Waipaoa River basin, New Zealand. Water Resources
746 Research 36, 1129-1142.
747 Hicks, D.M., Gomez, B., Trustrum, N.A., 2004. Event suspended sediment
748 characteristics and the generation of hyperpycnal plumes at river mouths: east

749 coast continental margin, North Island, New Zealand. Journal of Geology 112,
750 471-485.
751 Kniskern, T.A., 2007. Shelf sediment dispersal mechanisms and deposition on the
752 Waiapu River Shelf, New Zealand. PhD Dissertation, School of Marine
753 Science, College of William and Mary, Gloucester Point, VA, USA.
754 Kniskern, T.A., Kuehl, S.A., Harris, C.K., Carter, L., 2009. Sediment accumulation
755 patterns and fine-scale strata formation on the Waiapu River shelf, New
756 Zealand. Marine Geology (in press).
757 Lewis, K.B., Lallemand, S.E., Carter, L., 2004. Collapse in a Quaternary shelf basin
758 off East Cape, New Zealand: evidence for passage of a subducted seamount
759 inboard of the Ruatoria giant avalanche. New Zealand Journal of Geology and
760 Geophysics 47, 415-429.
761 Ma, Y., Wright, L.D., Friedrichs, C.T., 2008. Observations of Sediment Transport on
762 the Continental Shelf off the Mouth of the Waiapu River, New Zealand:
763 Evidence for Current-Supported Gravity Flows. Continental Shelf Research 28,
764 516-532.
765 Ma, Y., 2009. Continental shelf sediment transport and depositional processes on an
766 energetic, active margin: the Waiapu River shelf, New Zealand. PhD
767 Dissertation, School of Marine Science, College of William and Mary,
768 Gloucester Point, VA, USA.

769 Milliman, J.D., Syvitski J.P.M., 1992. Geomorphic/tectonic control of sediment
770 discharge to the ocean: the importance of small mountainous rivers. The
771 Journal of Geology 100, 525-544.
772 Mulder, T., Syvitski, J.P.M., 1995. Turbidity currents generated at river mouths
773 during exceptional discharges to the world oceans, Journal of Geology 103,
774 285-299.
775 Nittrouer, C.A., 1999. STRATFORM: overview of its design and syhthesis of its
776 results. Marine Geology 32, 85-113.
777 Nittrouer, C.A., Miserocchi, S., Trincardi, A.F., 2004. The PASTA project:
778 investigationg of Po and Apennine sediment transport and accumulation.
779 Oceanography 107, 46-57.
780 Ogston, A.S., Cacchione, D.A., Sternberg, R.W., Kineke, G.C., 2000. Observations of
781 storm and river flood-driven sediment transport on the northern California
782 continental shelf. Continental Shelf Research 20, 2141-2162.
783 Orpin, A.R., Carter, L., Kuehl, S.A., Trustrum, N.A., Lewis, K.B., Alexander, C.R.,
784 Gomez, B., 2002. Deposition from very high sediment yield New Zealand
785 river is captured in upper margin basins. MARGINS Newsletter 9, 1-4.
786 Scully, M.E., Friedrichs, C.T., Wright, L.D., 2002. Field support for an analytical
787 model of critically-stratified gravity-driven sediment transport and deposition
788 on the Eel River continental shelf, Northern California. Continental Shelf
789 Research 22, 1951-1974.

790 Scully, M.E., Friedrichs, C.T., Wright, L.D., 2003. Numerical modeling of
791 gravity-driven sediment transport and deposition on an energetic continental
792 shelf: Eel River, Northern California. Journal of Geophysical Research
793 108(C4), 17-1 – 17-14.
794 Tolman, H., 2002. User manual and system documentation of WAVEWATCH-III
795 version 2.22. NOAA/NWS/NCEP/MMAB Technical Note 222, pp. 133.
796 Traykovski, P., Geyer, W.R., Irish, J.D., Lynch, J.F., 2000. The role of wave-induced
797 density-driven fluid mud flows for cross-shelf transport on the Eel River
798 continental shelf. Continental Shelf Research 20, 2113-2140.
799 Traykovski, P., Wiberg, P.L., Geyer, W.R., 2007. Observations and modeling of
800 wave-supported sediment gravity flows on the Po prodelta and comparison to
801 prior observations from the Eel shelf. Continental Shelf Research 27, 375-399.
802 Trembanis, A.C., Friedrichs, C.T., Richardson, M., Traykovski, P.A., Howd, P., 2007.
803 Predicting seabed burial of cylinders by wave-induced scour: application to
804 the sandy inner shelf off Forida and Massachusetts. IEEE journal of Oceanic
805 Engineering 32 (1), 167-183.
806 Trowbridge, J.H., Kineke, G.C., 1994. Structure and dynamics of fluid muds on the
807 Amazon continental shelf. Journal of Geophysical Research 99, 865-874.
808 Wadman, H.M., McNinch, J.E., 2008. Spatial variation on the inner shelf of a high
809 yield river, Waiapu River, New Zealand: Implications for fine sediment
810 dispersal and preservation. Continental Shelf Research 28, 865-886.

811 Wheatcroft, R.A., 2000. Oceanic flood sedimentation: a new perspective. Continental
812 Shelf Research 20, 2059-2066.
813 Wright, L.D., Wiseman, W.J., Yang, Z.S., Bornhold, B.D., Keller, G.H., Prior, D.B.,
814 Suhayda, J.N., 1990. Processes of marine dispersal and deposition of
815 suspended silts off the modern mouth of the Huanghe (Yellow River).
816 Continental Shelf Research 10 (1), 1-40.
817 Wright, L.D., Kim, S.C., Friedrichs, C.T., 1999. Across-shelf variations in bed
818 roughness, bed stress and sediment suspension on the northern California shelf.
819 Marine Geology 154 (1-4), 99-115.
820 Wright, L.D., Friedrichs, C.T., Kim, S.C., Scully, M.E., 2001. Effects of ambient
821 currents and waves on gravity-driven sediment transport on continental
822 shelves, Marine Geology 175, 25-45.
823 Wright, L.D., Friedrichs, C.T., 2006. Gravity driven sediment transport on continental
824 shelves: A status report. Continental Shelf Research 26, 2092-2107.
825

826 FIGURE CAPTIONS

827

828 Figure 1. Study area of the Waiapu continental shelf (with bathymetry), northern
829 island of the New Zealand. Two tripods (from Ma et al., 2008) at 40-m and 60-m
830 isobaths are shown as triangles. The domain of 2-D gravity-driven flow model is
831 shown as the bold square, which covers an area of ~29 km × 25 km. The location of
832 the NOAA WAVEWATCH-III global model node used for wind and wave forcing is
833 shown as a square.

834

835 Figure 2. Waiapu shelf coring locations and resulting sediment accumulation patterns
836 based on ^{7}Be (upper, from Kniskern, 2007) and ^{210}Pb (lower, from Kniskern et al.,
837 2009). ^{7}Be indicates that sedimentation over 6-months previous to May 2004 was
838 mainly confined to depths shallower than 80 m, but ^{210}Pb shows a high long-term
839 (100 year) sedimentation rate between the 60-m and 120-m isobaths in a pattern
840 oriented oblique to the isobaths. (Also shown in the lower figure are fault and fold
841 lines delineating the Waiapu River shelf basin from Lewis et al. (2004)).

842

843 Figure 3. a) Root mean square wave height (H_{rms}) and b) along-shelf mean current
844 velocity from ADV tripod observations at 60-m isobath (black), along with calibrated
845 NOAA WAVEWATCH III ocean wave model hindcasts of a) H_{rms} and b) current
846 velocity (gray).

847

848 Figure 4. Along-shelf distribution of fluvial sediment input off the Waiapu River
849 mouth for the base-case model run.
850
851 Figure 5. Model inputs during September 2003 to May 2004 low energy period (LEP)
852 and during May to Septebmer 2004 high energy period (HEP): a) Root mean square
853 wave height (H_{rms}) and b) current velocity (v_c) from calibrated NWW3 wave and wind
854 hindcasts; and c) sediment discharge (Q_s) from the Waiapu River based on 0.23 times
855 the rating curve prediction from Hicks et al. (2004) using water discharge provided by
856 the Gisborne District Council. d) Daily median values for the depth at which model v_c
857 first exceeded the r.m.s. amplitude of near-bed wave orbital velocity (u_w).
858
859 Figure 6. Time series of gravity-driven flow at the 60-m tripod site from May to July
860 2004. The solid line is observed velocity; the dashed line is from the two-dimensional
861 model forced by NWW3 output. The observed gravity-driven velocity is defined as
862 the across-shelf velocity observed 43 cm above the bed minus the across-shelf
863 velocity observed 26 m above the bed (data from Ma, 2009). Both time series were
864 passed through a 40 hour low-pass filter.
865
866 Figure 7. Modeled sediment deposition thickness during the low-energy portion (LEP)
867 from September 2003 to May 2004. Also shown is the smoothed bathymetry used to
868 calculate bed slope. The superimposed symbols (also shown in Fig. 2a) are observed
869 non-zero ^{7}Be activities from Kniskern (2007) (triangle = low, cross = medium, star =

high) and a dashed line from Kniskern (2007) delineating the inferred offshore extent of observed ^{7}Be. Inverted triangles indicate locations of Ma et al. (2008) tripods

Figure 8. Contour plot of the absolute value of bed slope calculated from the smoothed bathymetry (also shown). Inverted triangles indicate locations of Ma et al. (2008) tripods.

Figure 9. Modeled sediment deposition thickness during the high-energy portion (HEP) from May to August 2004. Also shown are smoothed bathymetric contours (in black) and the Kniskern et al. (2009) observed 3 cm/year sediment accumulation contours (in dark green) from Figure 2b. The two straight grey lines are along- and across-shelf profiles used in Figures 10 and 11. Inverted triangles indicate locations of Ma et al. (2008) tripods.

Figure 10. Comparisons of base case deposition (solid line) to (a) across- and (b) along-shelf deposition with no current (dashed line) and with zero along-shelf slope (dash-dotted line), and to (c) across- and (d) along-shelf deposition with uniform sediment input (dashed line) and with doubled sediment input (dash-dotted line). Component of bed slope in the direction of (e) across- and (f) along-shelf transect. Across-shelf gradient in bed slope ($\partial\alpha/\partial x$) along the (g) across- and (h) along-shelf transect. Locations of profiles are shown in Figure 9.

Figure 1. Study area of the Waiapu continental shelf (with bathymetry), northern island of the New Zealand. Two tripods (from Ma et al., 2008) at 40-m and 60-m isobaths are shown as triangles. The domain of 2-D gravity-driven flow model is shown as the bold square, which covers an area of ~29 km × 25 km. The location of the NOAA WAVEWATCH-III global model node used for wind and wave forcing is shown as a square.

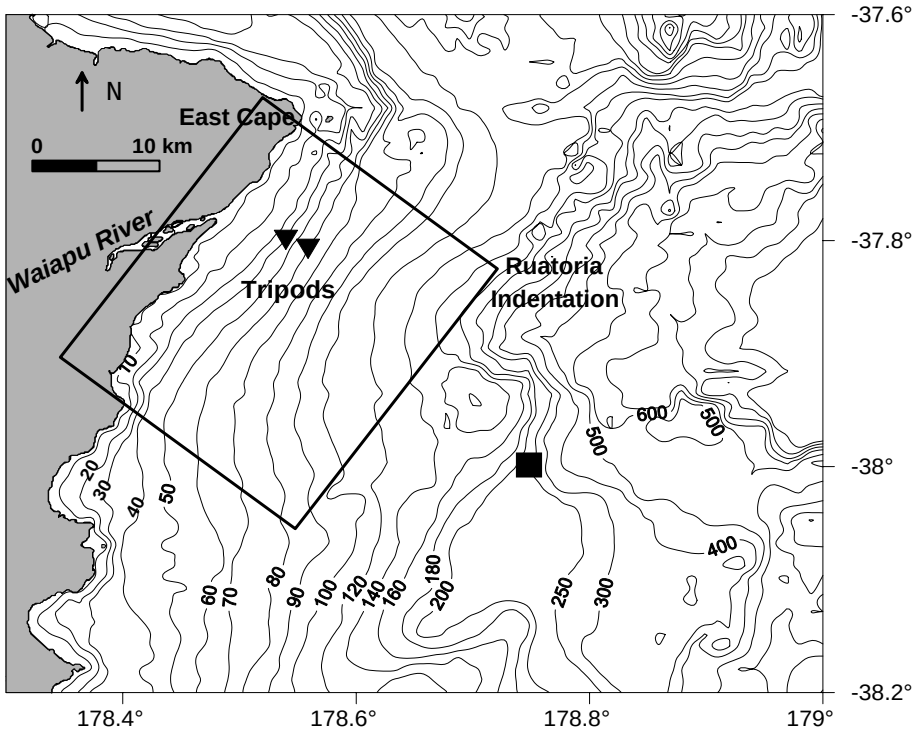

Figure 2. Waiapu shelf coring locations and resulting sediment accumulation patterns based on ^{7}Be (upper, from Kniskern, 2007) and ^{210}Pb (lower, from Kniskern et al., 2009). ^{7}Be indicates that sedimentation over 6-months previous to May 2004 was mainly confined to depths shallower than 80 m, but ^{210}Pb shows a high long-term (100 year) sedimentation rate between the 60-m and 120-m isobaths in a pattern oriented oblique to the isobaths. (Also shown in the lower figure are fault and fold lines delineating the Waiapu River shelf basin from Lewis et al. (2004)).

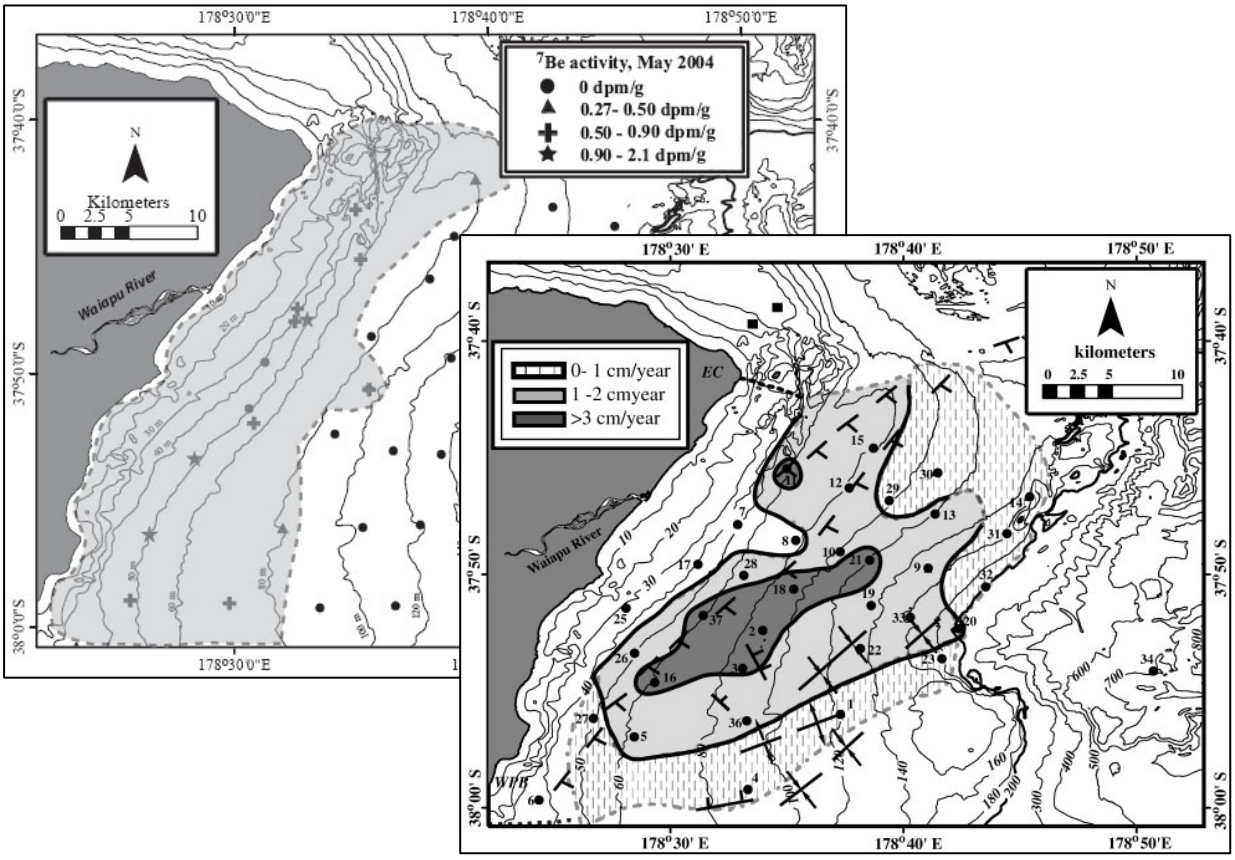

Figure 3. a) Root mean square wave height (H_{rms}) and b) along-shelf mean current velocity from ADV tripod observations at 60-m isobath (black), along with calibrated NOAA WAVEWATCH III ocean wave model hindcasts of a) H_{rms} and b) current velocity (gray).

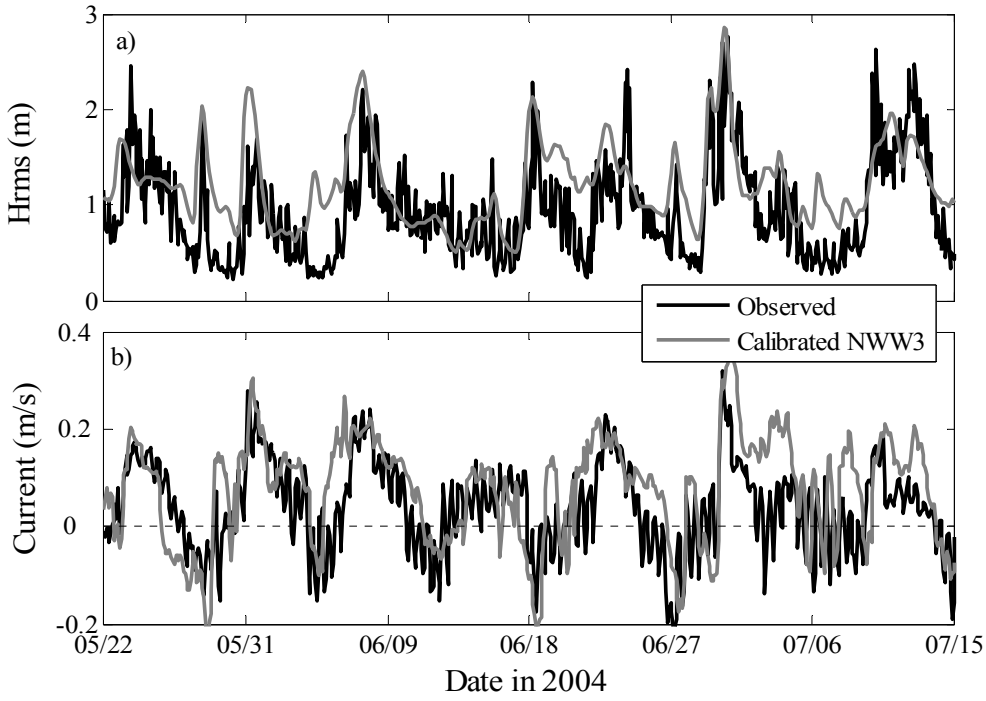

Figure 4. Along-shelf distribution of fluvial sediment input off the Waiapu River mouth for the base-case model run.

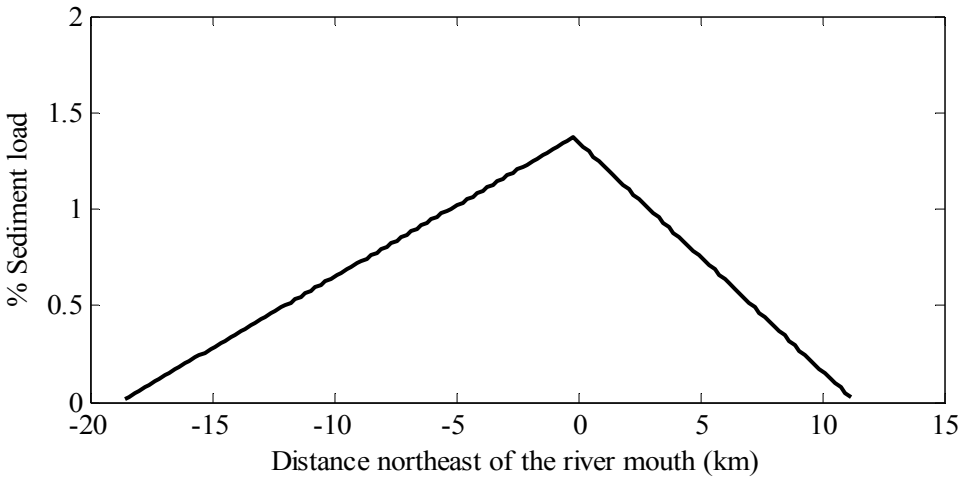

Figure 5. Model inputs during September 2003 to May 2004 low energy period (LEP) and during May to Septebmer 2004 high energy period (HEP): a) Root mean square wave height (*Hrms*) and b) current velocity (v_c) from calibrated NWW3 wave and wind hindcasts; and c) sediment discharge (*Qs*) from the Waiapu River based on 0.23 times the rating curve prediction from Hicks et al. (2004) using water discharge provided by the Gisborne District Council. d) Daily median values for the depth at which model v_c first exceeded the r.m.s. amplitude of near-bed wave orbital velocity (u_w).

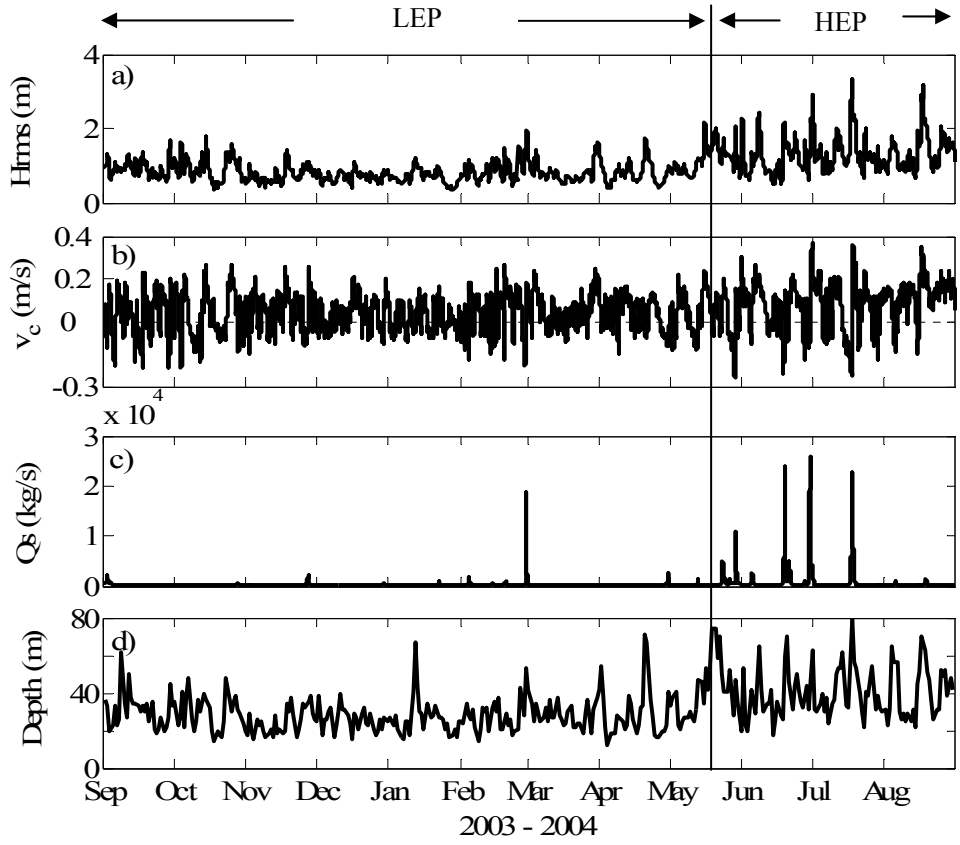

Figure 6. Time series of gravity-driven flow at the 60-m tripod site from May to July 2004. The solid line is observed velocity; the dashed line is from the two-dimensional model forced by NWW3 output. The observed gravity-driven velocity is defined as the across-shelf velocity observed 43 cm above the bed minus the across-shelf velocity observed 26 m above the bed (data from Ma, 2009). Both time series were passed through a 40 hour low-pass filter.

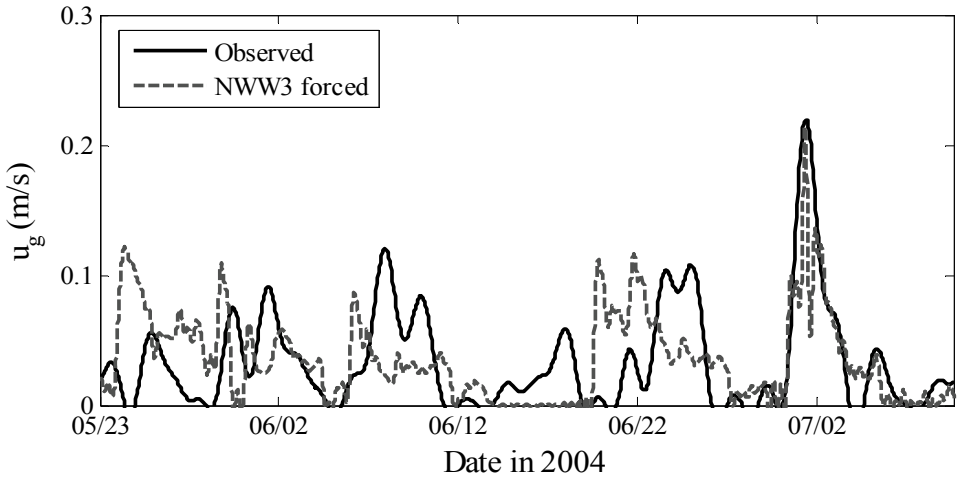

Figure 7. Modeled sediment deposition thickness during the low-energy portion (LEP) from September 2003 to May 2004. Also shown is the smoothed bathymetry used to calculate bed slope. The superimposed symbols (also shown in Fig. 2a) are observed non-zero ^{7}Be activities from Kniskern (2007) (triangle = low, cross = medium, star = high) and a dashed line from Kniskern (2007) delineating the inferred offshore extent of observed ^{7}Be. Inverted triangles indicate locations of Ma et al. (2008) tripods

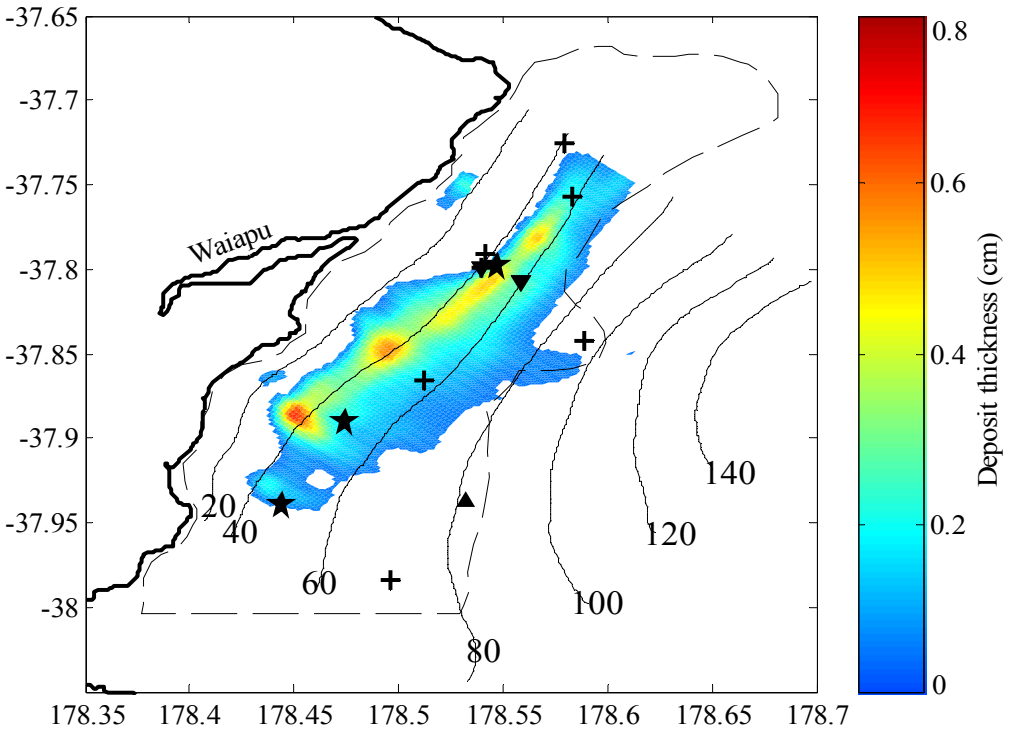

Figure 8. Contour plot of the absolute value of bed slope calculated from the smoothed bathymetry (also shown). Inverted triangles indicate locations of Ma et al. (2008) tripods.

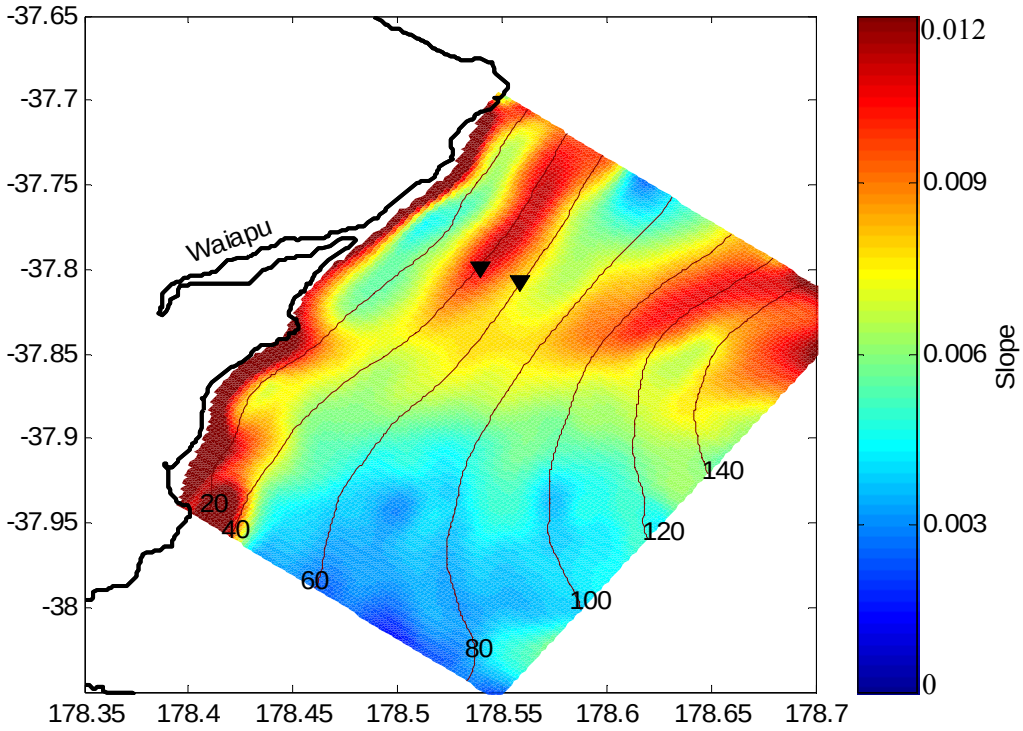

Figure 9. Modeled sediment deposition thickness during the high-energy portion (HEP) from May to August 2004. Also shown are smoothed bathymetric contours (in black) and the Kniskern et al. (2009) observed 3 cm/year sediment accumulation contours (in dark green) from Figure 2b. The two straight grey lines are along- and across-shelf profiles used in Figure 10. Inverted triangles indicate locations of Ma et al. (2008) tripods.

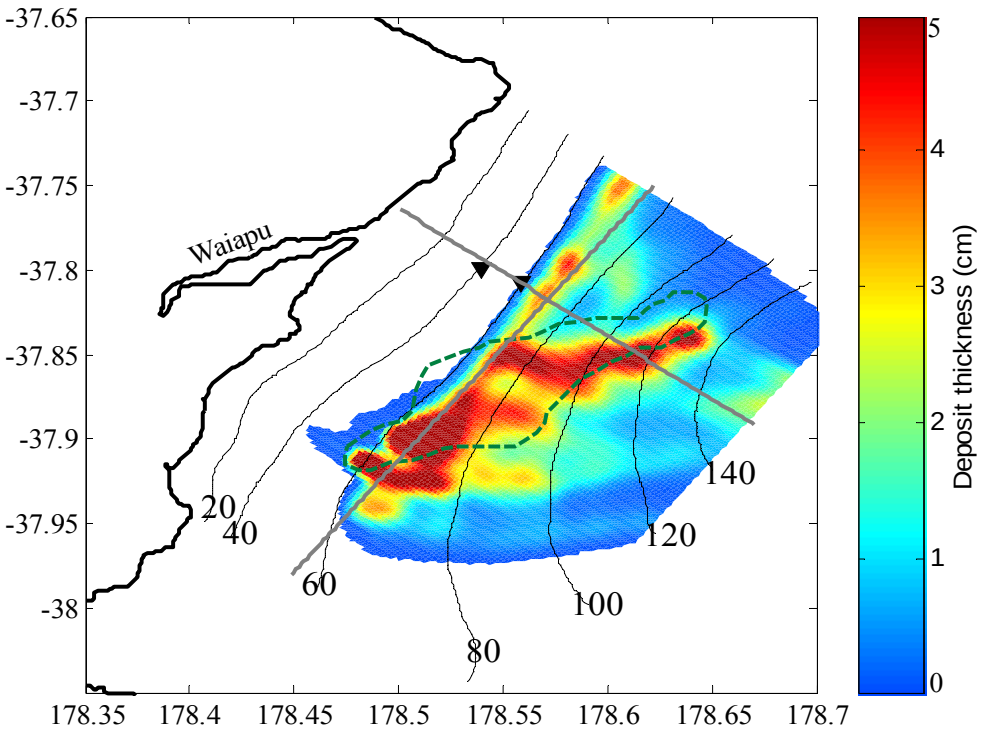

Figure 10. Comparisons of base case deposition (solid line) to (a) across- and (b) along-shelf deposition with no current (dashed line) and with zero along-shelf slope (dotted line), and to (c) across- and (d) along-shelf deposition with uniform sediment input (dashed line) and with doubled sediment input (dotted line). Component of bed slope in the direction of (e) across- and (f) along-shelf transect. Across-shelf gradient in bed slope ($\partial\alpha/\partial x$) along the (g) across- and (h) along-shelf transect. Locations of profiles are shown in Figure 9.